Aalborg Universitet

AALBORG UNIVERSITY
DENMARK

Transfer Learning for Adapting Battery State-of-Health Estimation from Laboratory to Field Operation

Vilsen, Søren Byg; Stroe, Daniel-Ioan

Transfer Learning for Adapting Battery State-of-Health Estimation from Laboratory to Field Operation

SØREN B. VILSEN[1], (Member, IEEE), and DANIEL-IOAN STROE[2], (Member, IEEE).
[1]Department of Mathematical Sciences, Aalborg University, Aalborg, Denmark (e-mail: svilsen@math.aau.dk)
[2]Department of Energy Technology, Aalborg University, Aalborg, Denmark (e-mail: dis@et.aau.dk)

Corresponding author: Søren B. Vilsen (e-mail: svilsen@math.aau.dk).

ABSTRACT The importance of accurate estimation of the state-of-health (SOH) for Lithium-ion (Li-ion) batteries is going to increase as Li-ion batteries become more integrated into daily life. As the reliance on Li-ion batteries increases so does the need for battery pack size optimisation and the extension of battery lifetime. Data-driven methods for estimation of the SOH of Li-ion batteries have shown to have good performance under laboratory conditions, but often fail to achieve similar performance when used in real life applications. This is a consequence of the field data seldomly matching the laboratory data, which is a necessary condition of most data-driven methods. A method which aims to account for discrepancies between laboratory and field data is transfer learning. This paper shows how the transfer learning algorithm kernel mean matching can be used to transfer both multiple linear regression (MLR) and bootstrapped random vector functional link (BRVFL) models from the laboratory to the field. It is shown that these methods can achieve mean absolute percentage errors (MAPE's) smaller than 1% on both laboratory and field data simultaneously.

INDEX TERMS Bagging random vector functional link neural networks, feature extraction, Lithium-ion batteries, multiple linear regression, transfer learning

I. INTRODUCTION

THERE has been an increase in the use of Lithium-ion (Li-ion) batteries in daily life both through the deployment of more electric vehicles and in grid-connected residential energy storage systems. It is, therefore, in the best interest of manufacturers and end users to optimise the size of the battery packs and the lifetime of the battery from both an environmental and economic perspective. In order to achieve this goal, it is important to accurately ascertain the health of the battery at every moment during its operation. Nevertheless, accurately estimating the battery state-of-health (SOH) often requires extensive and expensive laboratory experiments, which can quickly become obsolete.

Estimation of the SOH of a battery usually falls into one of two categories: (1) physics-driven methods, or (2) data-driven methods. The physics-driven methods aim to model the the internal states of the battery using theory of physics, chemistry, and electrical circuits. Among the most popular approaches are the electrochemical models consisting of par- tial differential equations, which model the internal battery components and their interactions [1], [2], and equivalent electric circuit (EEC), which relate battery current to the voltage through a series of simple circuit elements (e.g., re- sistors, capacitors, voltage sources etc.) [3]–[7]. While these methods can be very accurate, they require very large fully factorial experimental designs to determine the necessary pa- rameter [8]. Full factorial experimental designs are necessary to account for all possible battery parameter (e.g., capacity. resistance etc.) dependencies such as temperature, SOC, and level of degradation. As an alternative, complex Kalman filters have had some success in estimating the battery SOH [9]–[17]. However, due to their intrinsic properties, a singular solution can not always be ensured to exist, and even if recursive estimation is used to account for this potential problem, they require constant monitoring of the battery. In recent years, there has been an increasing interest towards more data-driven methods, as they require little to no expert knowledge and are usually only dependent on the input and

the output of the system. Among data-driven methods three of the more popular choices are: (1) support vector machines (SVM) [18]–[21], (2) Gaussian process regression (GPR) [22]–[28], and (3) artificial neural networks (ANN) [29]–[33]. While these methods are black-box methods offering little to no insight on the how/why the degradation occurs, they can achieve errors as small as 0.5%. However, a lot of data is required for ensuring small estimation errors. Therefore, alternative methods have been proposed which extract more relevant features from the raw measurements, and use simpler models like multiple linear regression (MLR) [34], random vector functional link neural networks [35]–[39] (RVFL), extreme learning machines [40], [41]. These methods require much less data, while still achieving errors smaller than 2%. Lastly, it has been shown that incremental capacity (IC) can be related to the SOH by extracting relevant features from the IC curves and modelling the relationship between features and SOH using MLR. However, this requires the IC curves to be known. It has been shown that the IC curves can be found using data-driven methods like SVM and ANN [42]–[48]. It has been shown that the methods based on the re-constructed IC curves can achieve errors as low as 0.5%, even in real-life application [47]. Furthermore, very recent advancements have shown that a hybrid EEC and ANN approach could achieve errors smaller than 1% [48]. However, the performance comes at the cost of a more complicated feature extraction due to the IC curve re-construction. A general disadvantage of the data-driven methods (including the hybrid methods) is that the laboratory data on which the models are trained needs to resemble the intended application. If the application deviates even slightly (dependent on the method) from the laboratory experiments, then the predictions of the model cannot be trusted. That is, if the usage pattern in application changes, then the laboratory experiments needs to be re-performed using this new pattern. An important question is: Can this be avoided? A possible solution is transductive transfer learning.

Transfer learning aims to reduce the amount of data re-collection by accounting for the fact that the model is going to be used in a different context than where it was trained [49]. That is, when training the model, transfer learning tries to account for the differences between the features used to train the model, and the features observed in the application. While some researchers have considered transfer learning for battery SOH and remaining useful life (RUL) estimation [50], [51], they have focused on very complicated recurrent neural network models necessitating large training sets. Furthermore, the type of transfer learning used still requires knowledge of the SOH on the the field operated batteries (in this context called the target domain). Therefore, the aim of the this paper is to show that much simpler SOH modelsbuild and tested using laboratory ageing experiments can be transferred to field operated batteries, without the need for SOH measurements in the target domain. This was achieved by transferring the models using a type of (transductive) transfer learning called kernel mean matching [52].

The remainder of the paper is structured as follows: First the experimental setup and the results of the laboratory experiments are presented in Section II-A. After which, three strategies for extracting features are then presented in Section II-B. These features are used to estimate the SOH in Section II-C. Section II-D shows how the proposed models can be transferred from the domain in which they are to be trained (the laboratory) to the domain where they are to be applied (the field). The results of the transferred models can be found in Section III, and a discussion of the approach follows in Section IV. Lastly, while SOH can be measured on two fronts capacity and power, the focus in this paper will be on capacity degradation. That is, from this point forward SOH estimation will refer to capacity estimation (though the ideas outlined in this paper will also extend to SOH modelling in terms of power or resistance).

II. MATERIALS AND METHODS
A. EXPERIMENTAL SETUP
1) Battery and forklift operation
In this work, Li-ion battery cells with a nominal capacity of 180 Ah and a nominal voltage of 3.3 V were considered. The cells are based on a graphite anode and a lithium iron phosphate cathode. Battery packs, composed of these cells, had been deployed in the field, in three forklifts, which were placed in the back of trucks around Europe and used to move heavy pallets throughout the day, and charged every few days. A representative one-week operation profile for the three forklifts is presented in Fig.'s 1 and 2. The figure shows that the operation of the forklifts leads to mostly short and shallow cycles.
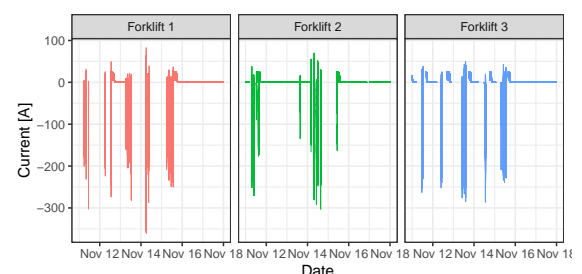

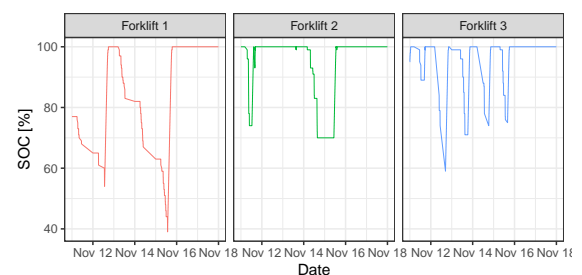**FIGURE 1.** Battery load profile during one-week of forklift operation.

FIGURE 2. Battery SOC profile during one-week of forklift operation.

Furthermore, throughout the operation of these forklifts there have only been a few deep cycles (i.e. with a depth of discharge larger than 80%) and subsequently constant current charging allowing for an approximation of the battery charging capacity in only a very few cases. Fig. 3 shows the approximate forklift battery charging capacity against the full equivalent cycles (FECs). As one can observe in the figure, the amount of degradation experienced by the battery in the forklifts is minimal – between 0.5 and 1% of degradation during the entire analysed operation period, approximately 17 months. Lastly, the operation of the battery allowed for the calculation of an approximate capacity at only four points in time for Forklift 2 and six for Forklift 3.

2) Laboratory Ageing Tests

Due to the nature of the usage of the batteries, with irregular deep discharges, creating a comprehensive battery degradation model would be difficult. Therefore, a total of six accelerated ageing tests were conducted; three concerning calendar ageing, and three cycle ageing. For both calendar and cycle ageing, the batteries were aged at 35, 40, and 45°C to capture the effect of temperature on the degradation. The batteries used to analyse the effects of calendar ageing were stored at 90% SOC, as this was the average SOC the forklifts were subjected when they were in idling mode. Every two weeks a reference performance test is performed to measure the capacity of the batteries and to quantify their incremental degradation.

Fig. 4 presents the capacity decrease of the cells during calendar ageing at the three ageing temperatures and 90% SOC. From these results, it is seen that the increase in the idling temperature from 35 ^{o}C to 45 ^{o}C, does not have a large influence in the capacity fade behavior of the cells (i.e., maximum 5% difference after 15 months of idling between the considered temperatures).

The batteries used for cycle ageing were subjected to a load profile created using the first six months of battery operation
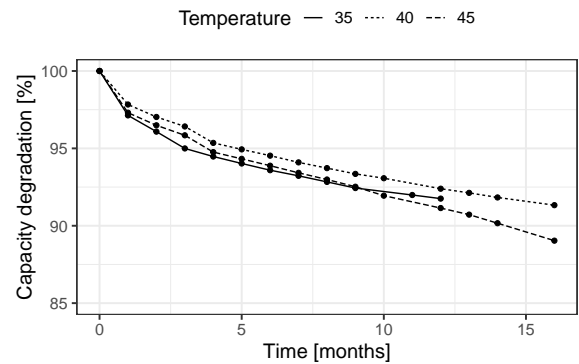

FIGURE 4. The capacity degradation due to calendar ageing of three batteries aged at a 35, 40, and 45°C shown against time in months.

in the forklifts. The profile was created by removing all idling periods (which account for more than 90% of the total operation) from the first six months of the of the battery operation in the forklifts, resulting in a profile of approximately 12 days. However, while the forklift during operation is subjected to the average current applied to the battery was 22 A, it has peaks above 350 A; due to current limitations of the laboratory battery test station, the current had to be kept below 50 A. This creates a possible discrepancy between not only the currents of the ageing profile and the actual forklift profile, but also their SOCs. In order to overcome this issue (i.e., SOC mismatch between the two profiles), whenever the current in the forklift profile exceeded 50 A (mainly during discharging), the ageing profile was limited to 50 A until the same SOC value was reached for both forklift and laboratory ageing profile. This ensured that the SOCs of the two profiles were identical. The aforementioned procedure, distilled the six months of forklift operation into the two-week profile, shown in Fig.'s 5 and 6, which was used to perform cycle ageing tests at three temperatures (i.e., 35, 40, and 45°C). After each round of cycle ageing (i.e. every two-weeks), a
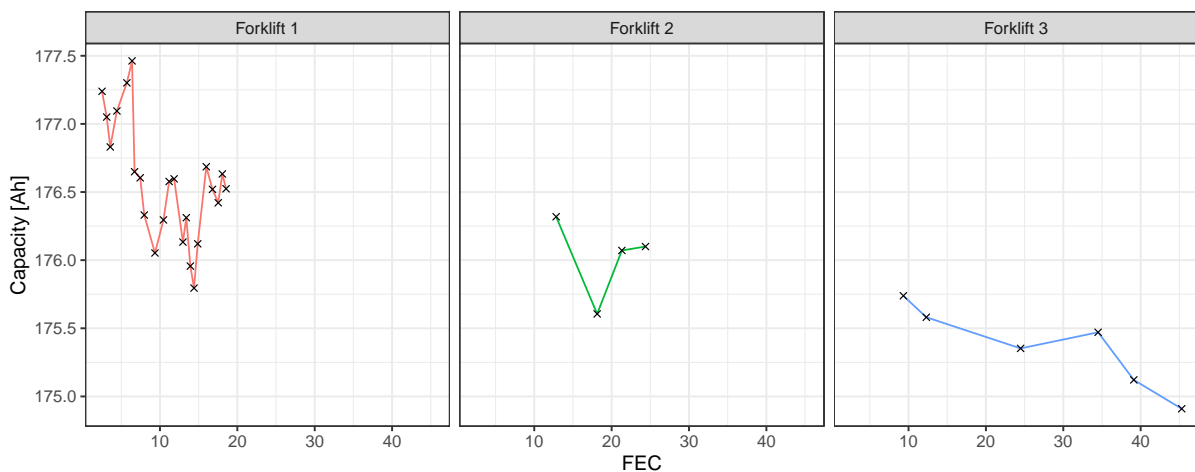

FIGURE 3. The approximate battery charging capacity shown against FEC for the three forklifts.

reference performance test was performed to measure the capacity of the batteries and to quantify their degradation.
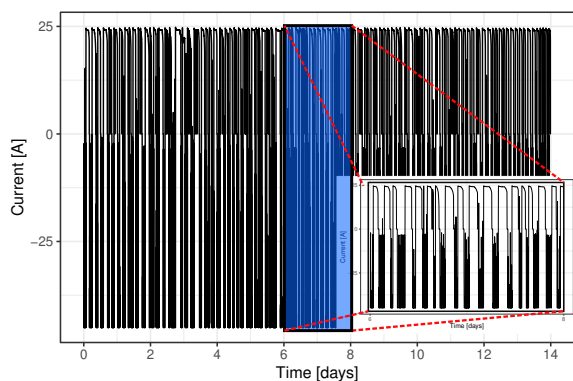

FIGURE 5. The current of the two week profile used to age the three batteries in the cycle experiment.
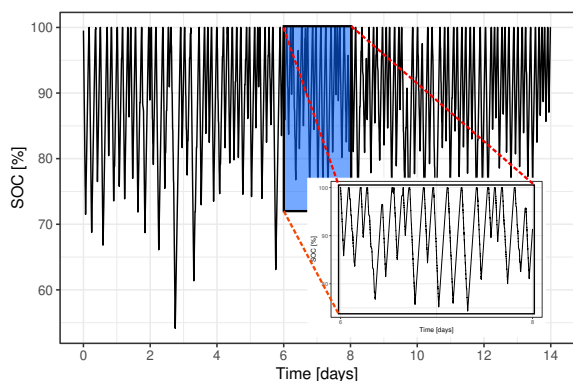

FIGURE 6. The SOC of the two week profile used to age the three batteries in the cycle experiment.

Fig. 7 shows the evolution of the capacity degradation, of the tested battery cells, during cycle ageing at the three ageing temperatures. It can be observed that the degradation behaviour of the three batteries is almost identical despite the 10^oC difference in the ageing temperature, which is similar to the results obtained for the calendar ageing. Furthermore, Fig. 7 illustrates that during the considered cycle aging experiment, the batteries were subjected to nearly 600 FECs, which resulted in approximately 10% capacity fade.

B. STATE-OF-HEALTH FEATURES

The aim of feature extraction is to take raw measurement data and distill this information into a set of variables, commonly called features, which are still able to accurately represent the raw measurements. A model is then created to establish a relationship between these features and the battery capacity (i.e. the SOH). Furthermore, the feature extraction methods, in this paper, are window based (similar to the methodology presented in [34]), i.e. a period (or window-size) will be specified and the features will be extracted using the raw measurements within this period.
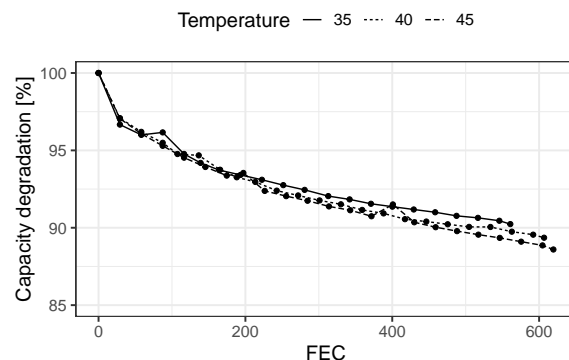

FIGURE 7. The capacity degradation due to cycle ageing of three batteries aged at a 35, 40, and 45°C shown against FEC.

The extracted features will be used to model the capacity measured during the reference performance tests performed at the end of every round of ageing of the battery cells. As every round of ageing will only have a single capacity measurement, it is natural to extract the features based on these rounds of ageing, i.e. the features on the ageing data will be extracted on a two-week basis.

The length of the period used to extract the features on the forklift data is not as important, as the period being large enough to yield consistent results. Preliminary extraction showed that an extraction period of one week yielded consistent results. Furthermore, due to the nature of the capacity measurements performed in the laboratory, the feature extraction from the forklift data has to be disjoint (i.e. they can not overlap).

The features extracted on both the ageing and forklift data will be based on three slightly different techniques: (1) simple descriptive statistics [34], (2) partial voltage charging [53], [54], and (3) online resistance extraction [55]. These methods were chosen because they can be performed in an "online" fashion using relatively little computing power.

1) Simple descriptive statistics

The descriptive statistics will be extracted from the raw voltage, current, and temperature profiles in every window in both the laboratory ageing and forklift data. The descriptive features give insight into the distribution of the voltage, current, and temperature. In the following sections the aim will be to link the change in these distributions to the degradation of the battery. The voltage, current, and temperature of window w will be denoted by $\boldsymbol{V}_w$, $\boldsymbol{I}_w$, and $\boldsymbol{T}_w$, respectively, and assumed to have length N (i.e. $\boldsymbol{V}_w$, $\boldsymbol{I}_w$, and $\boldsymbol{T}_w$ are vectors in $\mathbb{R}^N$). Furthermore, it will be assumed that the features for all previous windows, $1, 2, ..., w-1$ have already been extracted from the raw measurements.

In the following, a short description of each of the descriptive features, and how they are calculated for each window, is given:

- **Average** of the voltage, current, and temperature ($\boldsymbol{X}_w$ is used to represent either $\boldsymbol{V}_w$, $\boldsymbol{I}_w$, or $\boldsymbol{T}_w$): a measure
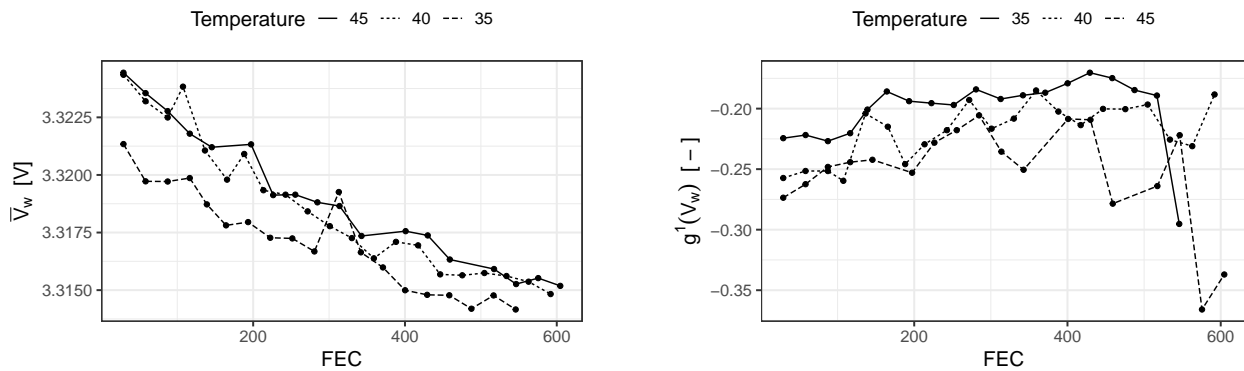
IEEE *Access*

FIGURE 8. Extracted features of the ageing data shown against FEC. The left panel shows the average voltage within each round of ageing, while the right panel shows the skewness of the voltage.

of center of a distribution, and is calculated as:

$$\bar{X}_w = \frac{1}{N} \sum_{n=1}^{N} X_{wn}$$

- **Standard deviation** of the voltage, current, and temperature ($\boldsymbol{X}_w$ is used to represent either $\boldsymbol{V}_w$, $\boldsymbol{I}_w$, or $\boldsymbol{T}_w$): a measure of deviation around the average (the square root of the average squared distance of every point from the center), and is calculated as

$$s(\boldsymbol{X}_w) = \left(\frac{1}{N-1} \sum_{n=1}^{N} (X_{wn} - \bar{X}_w)^2 \right)^{(1/2)}$$

- **Skewness** of the voltage and current ($\boldsymbol{X}_w$ is used to represent either $\boldsymbol{V}_w$ or $\boldsymbol{I}_w$): a measure of the asymmetry of the distribution (if its negative/positive it has larger left/right tails), and is calculated as:

$$g^1(\boldsymbol{X}_w) =$$
$$\frac{N}{(N-1)(N-2)} \frac{\sum_{n=1}^{N} (X_{wn} - \bar{X}_w)^3}{s(\boldsymbol{X}_w)^3}$$

- **Kurtosis** of the voltage and current ($\boldsymbol{X}_w$ is used to represent either $\boldsymbol{V}_w$ or $\boldsymbol{I}_w$): a measure of how large the tails of the distribution are when compared to a normal distribution (if it is larger/smaller than 0, the tails are larger/smaller than those of a normal distribution), and is calculated as:

$$g^2(\boldsymbol{X}_w) = \frac{1}{(N-2)(N-3)}$$
$$\times \left\{ \frac{(N+1)N}{(N-1)} \frac{\sum_{n=1}^{N} (X_{wn} - \bar{X}_w)^4}{s(\boldsymbol{X}_w)^4} \right.$$
$$\left. - 3(N-1)^2 \right\}$$

- **Maximum change** in the voltage and current ($\boldsymbol{X}_w$ is used to represent either $\boldsymbol{V}_w$, or $\boldsymbol{I}_w$): a measure of the largest change in the sequence (in the case of the voltage this will be related to the ohmic resistance, while for the

current it is related to the workload), and is calculated as:

$$\Delta \boldsymbol{X}_w = \max_{n \,\in\, \{1,2,...,N-1\}} \left(X_{w(n+1)} - X_{wn} \right)$$

- Cumulative full equivalence cycles (**FEC**): a measure of the through-put normalised by the capacity of the battery cell, and is calculated as:

$$\text{FEC}_w = \text{FEC}_{w-1} + \frac{1}{2Q_{nominal}} \sum_{n=1}^{N} \frac{|I_{wn}|}{3600},$$

where FEC_{w-1} is the FEC of the previous window (with $\text{FEC}_0 = 0$), and $Q_{nominal}$ is the nominal capacity of the battery (in this case the nominal capacity is 180).

Fig. 8 shows two examples of the features extracted from the ageing data against FEC. The left panel shows the average voltage, it is clear that there is a decreasing trend in the average voltage as a function of the FEC, while there seems to be nearly no effect of the ageing on the skewness of the voltage distribution, as seen on the right panel. Furthermore, the panels show that the temperature does not seem to have an effect on the shape of these trend lines, only shifting them up or down.

2) Partial voltage charging

As the battery cell degrades, the time it takes for cell to completely charge from empty to full will naturally decrease, i.e. the time it takes for the cell to go from its lower to its upper voltage limits will decrease, as depicted in Fig. 10. Furthermore, it has been shown in [53], [54] that it is not necessary to observe the entire voltage curve from its absolute lower limit to its absolute upper limit, but calculating through-put in a restricted voltage window from V_{low} to V_{high} (shown as the red horizontal lines in Fig. 10) will be proportional to the calculating the capacity across the entire voltage curve.

If the extraction of these reduced capacity measurements, $\boldsymbol{Q}_w$, are to be performed from a dynamic profile, the current needs to be consistent as the voltage passes through the defined voltage limits, as it is well known that the capacity
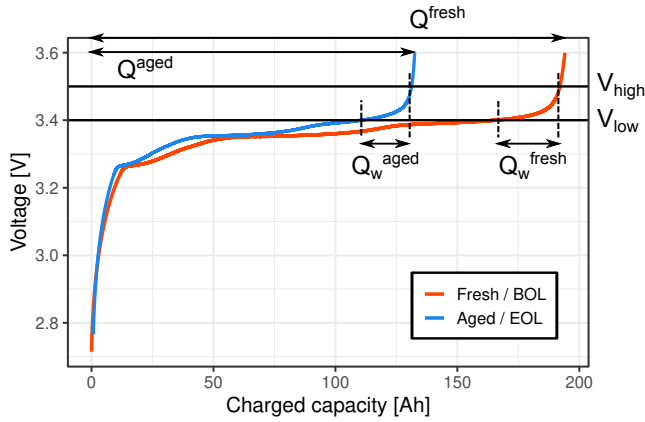
5

FIGURE 10. Exemplification of the partial voltage charging for a fresh and aged cell; the partial voltage interval lays between V_{low} and V_{high}.

is heavily dependent on the current. In real-life applications, the main difficulty of this method is to identify periods of time where the current is consistent, i.e. periods where the current profile repeats at different moments during the battery operation through its life. Luckily, the charging procedure of the forklifts and, therefore, the ageing profile, is consistent. This consistency allows for the extraction of $\boldsymbol{Q}_w$ every time the battery is fully charged, yielding multiple extracted $\boldsymbol{Q}_w$ values for every window in both the ageing and forklift data. After these features have been extracted, they will be summarised within each window by taking the average and standard deviation, denoted $\bar{Q}_w$ and $s(\boldsymbol{Q}_w)$, respectively.

The average and standard deviation of the extracted $\boldsymbol{Q}_w$ values for the ageing profile can be seen in the left- and right-hand panels of Fig. 9. As it can be observed, unlike the descriptive features, the evolution of these features as function of FEC is dependent on the temperature (at least $\bar{Q}_w$). Furthermore, two things are worth mentioning: (1) the curve of $\bar{Q}_w$ seems to be flattening, which could become a problem if used for prediction (unless the measured capacity behaves in a similar fashion), and (2) the standard deviation, seen in the right panel of Fig. 9, is increasing slowly overtime. That is, even though the voltage is passing through the same

voltage limits, the time is takes to pass through these limits becomes more inconsistent as the battery degrades.

3) Resistance

It has been shown that both the ohmic and internal resistance can be extracted, to within a reasonable accuracy, from dynamic profiles [55]. The battery resistance can be extracted from a dynamic profile by keeping very careful track of the following:

(1) Changes to the current: ΔI.
(2) The value of the voltage at the end of the last relaxation period V_s.
(3) Amount of time the battery was relaxed ΔT_{relax}.
(4) The length of the previous pulse $\Delta T_{previous}$.
(5) The length of the current pulse $\Delta T_{current}$.

Requiring a relaxation period at least as long as the previous pulse, the resistance can be extracted using these five variables, as sketched in Fig. 11.
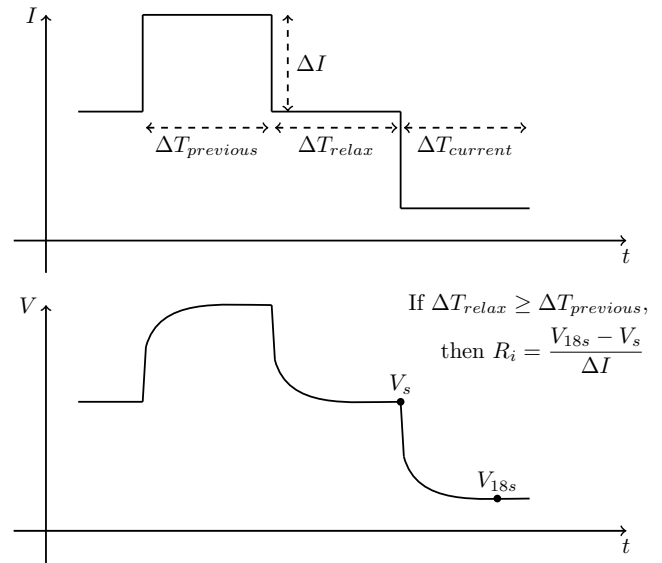

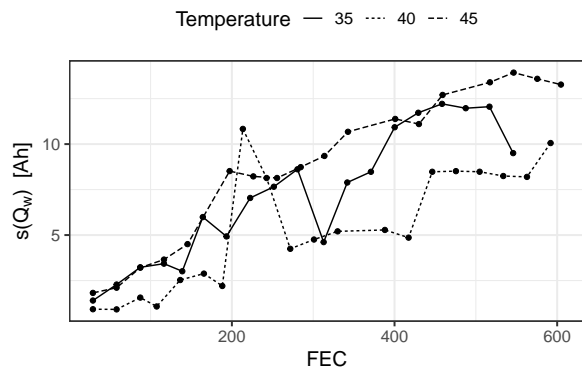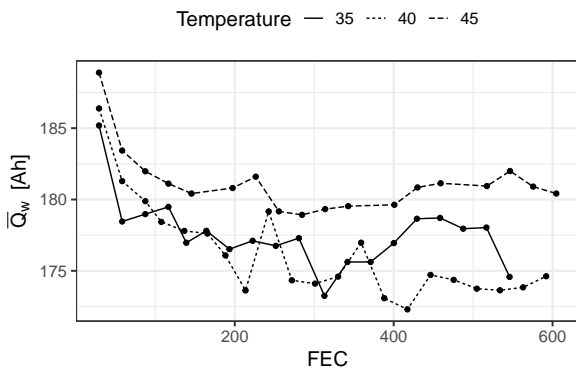**FIGURE 11.** Illustration of the resistance extraction method.

FIGURE 9. The average and the standard deviation of the extracted Q_w values against the FEC, shown in the left- and right-panel, respectively.
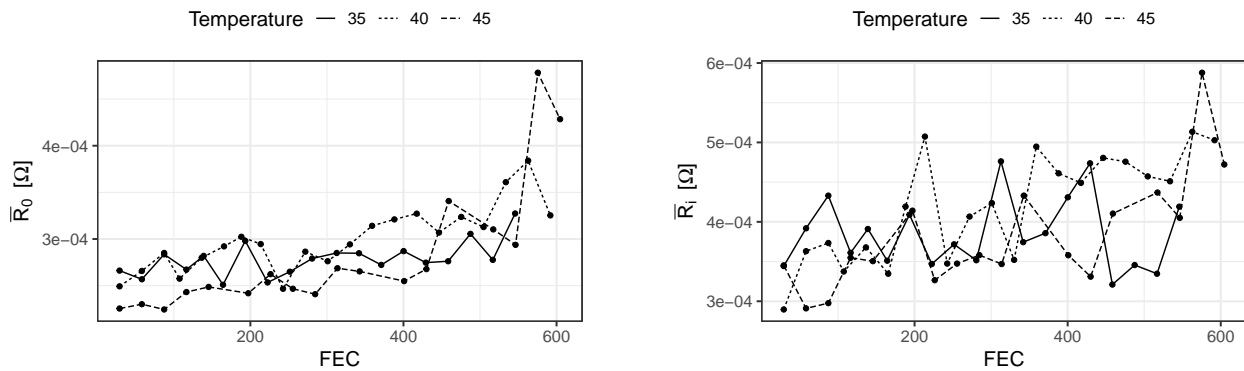
IEEE *Access*

FIGURE 12. The extracted ohmic and internal resistances against FEC, shown in the left- and right-hand panels, respectively.

To be more specific, requiring $\Delta T_{relax} \geq \Delta T_{previous}$, then the ohmic and internal resistances can be calculated as:

$$R_0 = \frac{V_{0.1s} - V_s}{\Delta I}, \quad \text{and} \quad R_i = \frac{V_{18s} - V_s}{\Delta I},$$

where $V_{0.1s}$ and V_{18s} is the voltage 0.1 seconds and 18 seconds after the initiation of the pulse, respectively.

Like the case of the partial voltage method, the ohmic and internal resistances can be extracted multiple times during every period (for both the ageing and forklift data). Therefore, they are summarised using the average and standard deviation to track the change in the distribution of the extracted features instead of the raw extracted values. These will be denoted as $\bar{R}_0$, $s(\boldsymbol{R}_0)$, $\bar{R}_i$, and $s(\boldsymbol{R}_i)$.

In Fig. 12 the average of the extracted ohmic and internal resistances are shown against FEC for every window of the ageing data. As would be expected, it shows that the average resistance (both ohmic and internal) increases as the battery degrades. Furthermore, the figures show that the overall trend of both the ohmic and internal resistance is not affected by temperature. Lastly, it seems the variation in the average extracted ohmic resistance is more stable than the average extracted internal resistance. It may be possible to stabilise the extracted internal resistance, by adding further restrictions on ΔT_{relax}, such as requiring it has to be larger than a minimum 15 seconds (i.e. $\Delta T_{relax} \geq \max\{\Delta T_{previous}, 15\}$). However, as $\bar{R}_i$ is just one of many SOH estimation features, it is not deemed unnecessary in the context of this paper.

C. STATE-OF-HEALTH MODELLING

As the aim of this paper is to transfer a model trained on the ageing data obtained in laboratory to the forklift data measured on the field, the modelling of state-of-health (SOH) should not be the focus. Therefore, the methods presented in this section are very simple, but with reasonably high accuracy.

It is assumed that the general SOH can be decomposed into two parts, the loss of capacity due to idling (calendar ageing), and the loss of capacity due to the cycling (cycle ageing).

Furthermore, it is assumed that this effect is additive. That is, the capacity in window w, denote Q_w, can be written as:

$$Q_w = Q_0 - \Delta Q_w^{(cy)} - \Delta Q_w^{(ca)}, \quad (1)$$

where Q_0 is the initial capacity, $\Delta Q_w^{(cy)}$ is the loss in capacity due to cycling, and $\Delta Q_w^{(ca)}$ is the loss in capacity due to calendar ageing.

The two components will be modelled separately as the loss in capacity due to each of these components, and the capacity is then predicted using Eq. (1). Lastly, the training and validation sets were created by making a random 70/30 split of the ageing data, where the 70% will used to train the models, and the 30% will be used to compare them.

1) Calendar model

Calendar ageing is mainly dependent on two factors: (1) the storage temperature, and (2) the SOC at which the battery is stored. As the storage SOC is going to be very consistent in the intended application (i.e., the forklifts), mostly between 90 and 100%, the storage SOC is going to be ignored as a variable. It has been shown in [56] that the relationship between storage time, temperature, and degradation should follow a power law, i.e. the logarithm of the loss in capacity due to calendar ageing, $\Delta Q_w^{(ca)}$, can be modelled as:

$$\log\left(\Delta Q_w^{(ca)}\right) = \eta_0 + \eta_1 \cdot w + \eta_2 \cdot T + \eta_3 \cdot w \cdot T, \quad (2)$$

where w is the (accumulated) time in storage measured in weeks, and T is the temperature measured in centigrade. Using the calendar aged laboratory data, presented in Fig. 4, the parameters were found by simple least squares estimation (see Table 1), and the mean absolute percentage error (MAPE) on the validation set was calculate as $\approx 0.4\%$.

TABLE 1. The estimated parameters of the power law model, seen in Eq. (2), used to estimate capacity loss due to calendar ageing.

η_0	η_1	η_2	η_3
2.101	0.113	-0.019	0.009

The results of the model described by Eq. (2) using the trained parameters of Table 1 can be seen in Fig. 13.

This article has been accepted for publication in a future issue of this journal, but has not been fully edited. Content may change prior to final publication. Citation information: DOI 10.1109/ACCESS.2022.3156657, IEEE Access

IEEE Access

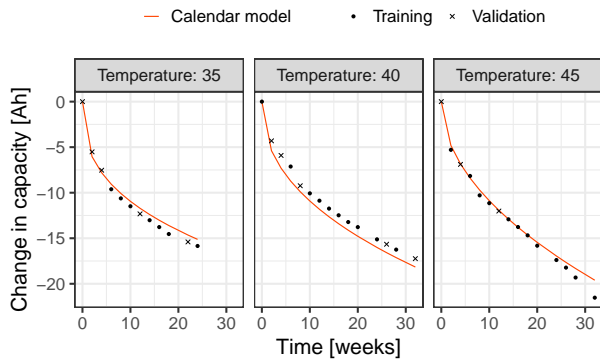Vilsen *et al.*: Preparation of paper for IEEE ACCESS

FIGURE 13. The change in capacity against the number of weeks in storage. The dots and crosses represent the training and validation sets, respectively. The trained power law model from Eq. (2) is shown in red.

2) Cycling model

Two methods will be compared when modelling the change in capacity due to cycling, $\Delta Q^{(cy)}$. The first method is a multiple linear regression model (MLR) [34], while the second is a bootstrap aggregated random vector functional link neural network (BRVFL) [41]. Before the models are trained feature reduction will be performed using principle components analysis (PCA) [57], [58]. Lastly, the two methods will be compared using cross-validation for each of the specified PCA thresholds.

Principle components analysis
PCA can be thought of as a linear transformation of the features, specifically a translation to the origin, followed by a rotation such that the new first coordinate explains most of the variation, the second explains the second most variation, and so on. A simple 2-dimensional example can be seen in Fig. 14, the left-hand panel shows the original features (simulated from a multivariate normal distribution with correlation 0.8), and the right-hand panel shows the PCA rotated features. The PCA coordinate axes are shown in both panels as the red and blue unit vectors.
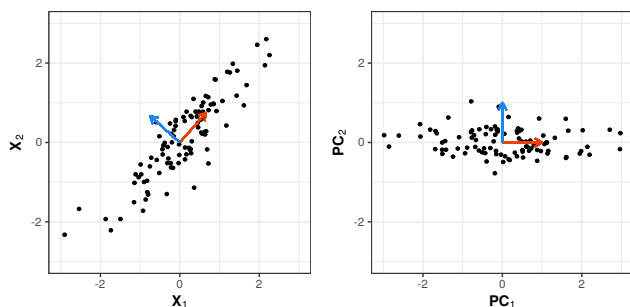

FIGURE 14. A 2-dimensional example of the linear transformation induced by principle components analysis.

If the features are stored in a matrix X, then the principle components can be found by diagonalisation of the matrix: $C = X^T X$. That is, by identifying the eigenvectors, V, and

eigenvalues, $\lambda_1, \lambda_2, ..., \lambda_M$, such that:

$$C = V^T \Lambda V,$$

where Λ is a diagonal matrix containing the eigenvalues $\lambda_1, \lambda_2, ..., \lambda_M$. The principle components correspond to the eigenvectors of C (i.e. V).

Using the matrix of principle components, the feature matrix can be rotated by simple matrix multiplication:

$$S = XV.$$

The elements of the diagonal matrix Λ are related to the amount of variation explained in the direction of the corresponding eigenvector, and found in numerically descending order, i.e. $|\lambda_1| > |\lambda_2| > ... > |\lambda_M|$. Thus, the features can be reduced by selecting the number of columns included in V when making the rotation.

It follows that to reduce the features, it becomes necessary to calculate the amount of variance explained by each of the principle components. If Σ is the covariance matrix of S, and σ_{mm} is the m'th diagonal element of Σ, then the proportion of the variation explained by the m'th principle component is:

$$p_m = \frac{\sigma_m}{\sigma_+},$$

where $\sigma_+ = \sum_{m=1}^{M} \sigma_{mm}$. As the principle vectors are arranged in descending order of variance they explained in the features, the cumulative sum of the proportions can be used to identify an index i such that the first i features will explain more variance than some specified lower limit t. That is, given t and the cumulative sum of the proportion of explained variance:

$$c_i = \sum_{m=1}^{i} p_m,$$

it is of interest to find the index, i, such that $c_{i-1} < t$, but $c_i \geq t$. Given this index i, the size of number of features is reduced as:

$$S^{(i)} = XV_{1:i},$$

where $V_{1:i}$ is the matrix of the first i columns of V. Note: from this point the superscript in $S^{(i)}$ will be generally be dropped to alleviate notation.

Multiple linear regression
Let $\Delta Q_w^{(cy)}$ be the change in capacity measured during the reference performance test, and $\boldsymbol{S}_w$ be the PCA reduced features corresponding the window w (this is the equivalent to the w'th round of ageing). A multiple linear regression (MLR) model assumes that the capacity can be modelled by a linear combination of the features, i.e.

$$\Delta Q_w^{(cy)} = \beta_0 + \sum_{j=1}^{i} S_{wj}\beta_j + \varepsilon,$$

where ε is assumed to follow a normal distribution with mean zero and standard deviation σ, β_0 is a common intercept, and

IEEE *Access*

β_j is the slope of feature j. That is, if all S_{wi} with $i \neq j$ are kept fixed and S_{wj} is increased by 1, then the response $\Delta Q_w^{(cy)}$ is expected to change by β_j.

Let $\mathcal{D}_{train} = \{(\Delta Q_1^{(cy)}, \boldsymbol{S}_1), (\Delta Q_2^{(cy)}, \boldsymbol{S}_2), ..., (\Delta Q_N^{(cy)}, \boldsymbol{S}_N)\}$ be a training set of N observation, then the regression coefficients, $\boldsymbol{\beta}$, can be trained by minimising the sum of squared errors:

$$\hat{\boldsymbol{\beta}} = \underset{\boldsymbol{\beta}}{\mathrm{argmin}} \left\{ \sum_{n=1}^{N} \left(y_n - \beta_0 - \sum_{j=1}^{i} S_{wj}\beta_j \right)^2 \right\}.$$

The solution to this optimisation problem can be found in closed form, using matrix notation the solution takes the form:

$$\tilde{\boldsymbol{\beta}} = \underset{\boldsymbol{\beta}}{\mathrm{argmin}} \left\{ ||\boldsymbol{Q}^{(cy)} - \tilde{S}\boldsymbol{\beta}||^2 \right\},$$

where $\boldsymbol{Q}^{(cy)} = \left(\Delta Q_1^{(cy)}, \Delta Q_2^{(cy)}, ..., \Delta Q_N^{(cy)} \right)^T$, S is the matrix containing the reduced features (with an observation in every row, and a feature in every column), and $\tilde{S} = [\mathbf{1} \quad S]$ (i.e. a column of 1's have been added representing the common intercept). The solution is found by differentiating $||\boldsymbol{Q}^{(cy)} - \tilde{S}\boldsymbol{\beta}||^2$, setting it equal to the zero vector, and isolating $\boldsymbol{\beta}$, which yields:

$$\hat{\boldsymbol{\beta}} = \left(\tilde{S}^T \tilde{S} \right)^{-1} \tilde{S}^T \boldsymbol{Q}^{(cy)}. \qquad (3)$$

Fig. 15 shows the change in capacity against the FEC for each of the three temperatures used in the accelerated ageing tests. The black dots correspond to the measured change in capacity in the training set, while the black crosses is the measured change in capacity in the validation set. The solid and dashed lines correspond to the estimated change in capacity using a PCA threshold of 95% and 100% (i.e. a

retention of 95% and 100% of the variation in the original features), respectively. The figure shows that there is nearly no difference between the two reduction thresholds with one very clear outlier seen when trying to predict the capacity around 200 FEC at a temperature of 45^oC. This can also be seen when comparing the mean absolute error (MAE) and MAPE on the validation sets in Table 2. The largest validation error was found at 45^oC with a value of 0.43% with a PCA threshold at 95% (with the second largest MAPE at 0.37%). However, as there is little to no difference between the two thresholds, it will enable the end user the choice of a smaller threshold yielding a larger reduction to the number of features used in the MLR. Either threshold showed good performance with errors less than 0.5%.

TABLE 2. Validation error between the measured and predicted change in capacity of the MLR model, shown for two PCA reduction thresholds at 95% and 100%, and each of the temperatures used to age the cells.

Temperature	PCA (95%)		PCA (100%)	
	MAE [Ah]	MAPE [%]	MAE [Ah]	MAPE [%]
35	0.61	0.34	0.18	0.10
40	0.55	0.31	0.55	0.31
45	0.77	0.43	0.37	0.21

Bagged random vector functional link

Random vector functional links (RVFL) are simple feed forward neural networks with a single hidden layer, where the bias and weights corresponding to the hidden neurons are randomised and kept fixed during the training phase, allowing for fast optimisation which can be solved in closed form.

The general structure of the RVFL can be seen in Fig. 16. The features are transformed using the randomly generated hidden layer, H, and the output layer is a concatenation of

Data • Training × Validation — Prediction (PCA (95%)) ···· Prediction (PCA (100%))

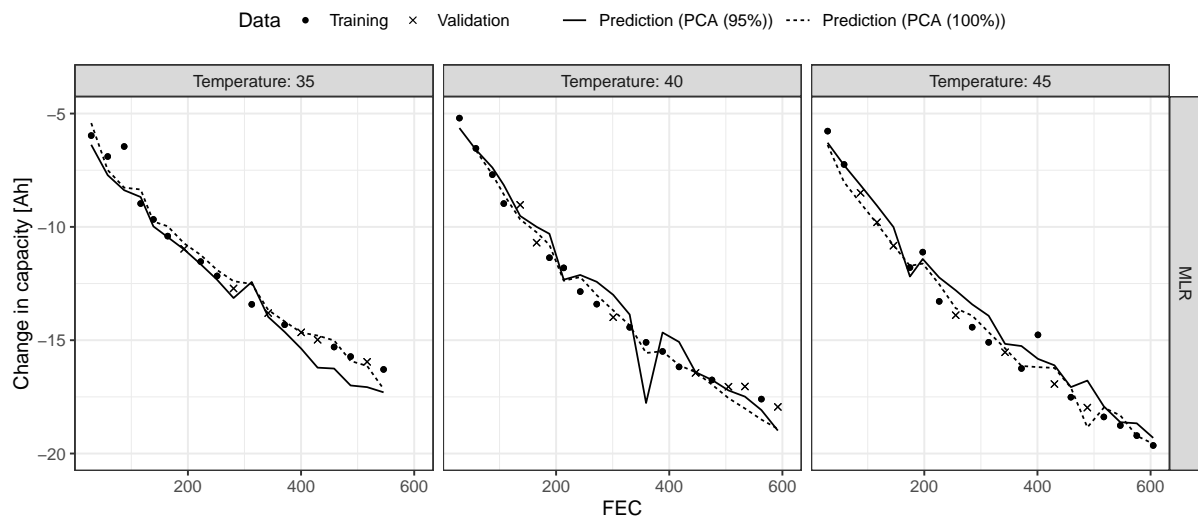**FIGURE 15.** Loss of capacity against FEC for each of the three temperatures in the ageing data. The dots are the measured change in capacity used to train the model, and the crosses is the measured change in capacity in the validation set. The solid and dashed lines are the estimated change in capacity by the trained MLR, referring to the PCA reduced features using 95% and 100% thresholds, respectively.
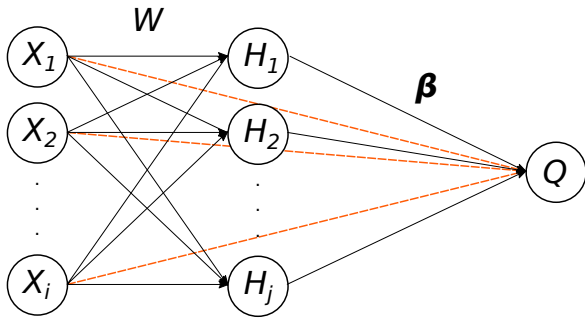
FIGURE 16. Graph representation of a random vector functional link neural network (RVFL).

the transformed features H and the reduced features S. That is, if the number of features in the reduced features is i and the number of hidden units is j, then the total number of units in the output layer is $i + j$.

If the concatenated features are arranged in a matrix $D = [S\ H]$, the solution can be found by minimising the penalised sum of squared errors:

$$\tilde{\boldsymbol{\beta}} = \left\{ \underset{\boldsymbol{\beta}}{\operatorname{argmin}} \, ||\boldsymbol{Q}^{(cy)} - D\boldsymbol{\beta}||^2 + \lambda ||\boldsymbol{\beta}||^2 \right\},$$

where λ is a regularisation constant, which should be chosen such that it minimises the out-of-sample error (this can be accomplished using k-fold cross-validation during training).

If $\lambda > 0$ the optimisation problem is a variant of ridge-regression, and the solution can be found in a similar fashion to what was described for the MLR:

$$\tilde{\boldsymbol{\beta}} = \left(D^T D + \lambda I_{i+j} \right)^{-1} D^T \boldsymbol{Q}^{(cy)}, \qquad (4)$$

where I_{i+j} is the identity matrix of size $i + j$. However, if λ is set to zero the solution will have to be found using the Moore-Penrose pseudoinverse, D^+, as:

$$\tilde{\boldsymbol{\beta}} = D^+ \boldsymbol{Q}^{(cy)}. \qquad (5)$$

Due the random nature of the RVFL method, various extension have been proposed to stabilise the random assignment of weights. Among the more promising variants are the sparse pre-trained RVFL (SP-RVFL) using a sparse auto-encoder to learn the hidden weights in an unsupervised fashion [38], ensemble deep RVFL (edRVFL) using an RVFL with multiple hidden layers each layer predicting the outcome [39], and bootstrap aggregated RVFL (BRVFL), which combines the random nature of the RVFL with a bootstrap aggregation [41].

The BRVFL is chosen as it is a simple extension offering more stability to the modelling process than the RVFL. When training the BRVFL, B bootstrap samples of the training set are created; bootstrap samples are samples of the same size as the training set, where each element has an equal probability of being chosen with replacement (i.e. the element is not removed if it is chosen and can, thus, be chosen again). A regular RVFL is then trained to each of the B bootstrap samples using Eq. (4). When predicting the capacity, initially

each of the B trained RVFL models will make a prediction, $\hat{Q}_{(1)}^{(cy)}, \hat{Q}_{(2)}^{(cy)}, ..., \hat{Q}_{(B)}^{(cy)}$, and the final prediction of the BRVFL model is then the average of these predictions:

$$\hat{Q}^{(cy)} = \frac{1}{B} \sum_{b=1}^{B} \hat{Q}_{(b)}^{(cy)}.$$

Fig. 17 shows the result of a trained BRVFL using 2500 bootstrap sample, a hidden layer with 200 neurons, and a $\lambda = 0.02$. The figure shows the change in capacity against the FEC for each of the three temperatures used in the accelerated ageing tests, where the black dots correspond to the measured change in capacity in the training set, and the black crosses is the measured change in capacity in the validation set. The solid and dashed lines correspond to the estimated change in capacity of the trained BRVFL using PCA thresholds of 95% and 100%, respectively. The figure shows very similar behaviour to the estimated capacities of the MLR for both thresholds. This is further supported by the validation errors seen in Table 3, showing very similar results to that of the MLR (though the MAPE's tend to be slightly smaller for the BRVFL).

TABLE 3. Validation error between the measured and predicted capacity of the BRVFL model, shown for two PCA reduction lower limits at 95% and 100%, and each of the temperatures used to age the cells.

Temperature	PCA (95%)		PCA (100%)	
	MAE [Ah]	MAPE [%]	MAE [Ah]	MAPE [%]
35	0.33	0.18	0.06	0.03
40	0.47	0.26	0.49	0.27
45	0.60	0.33	0.22	0.12

D. TRANSFER LEARNING

The aim of the paper is to take the SOH estimation models, which were parameterised using the laboratory ageing data, presented in Section II-C, and transfer these models to the field (i.e. the forklifts). Transference of these models cannot be done directly, because the distribution of the features extracted from the forklift data will not match those of the laboratory ageing data, as seen in Section II-A. This problem falls into a class of machine learning methods, called transductive transfer learning (TTL). In the context of TTL, the laboratory (where the ageing data is sampled from) is called the source domain, denoted $\mathcal{S}$, and the field (where the forklift data is sampled from) is called the target domain, denoted $\mathcal{T}$.

Restating the problem more mathematically, with $\boldsymbol{S}$ and $Q^{(cy)}$ denoting the features and capacity, the joint distributions of the source and target domains are not equal:

$$\mathbb{P}_{\mathcal{S}} \left(\boldsymbol{S}, Q^{(cy)} \right) \neq \mathbb{P}_{\mathcal{T}} \left(\boldsymbol{S}, Q^{(cy)} \right). \qquad (6)$$

TTL assumes that the conditional distributions in the source and target domains of the capacity given the features
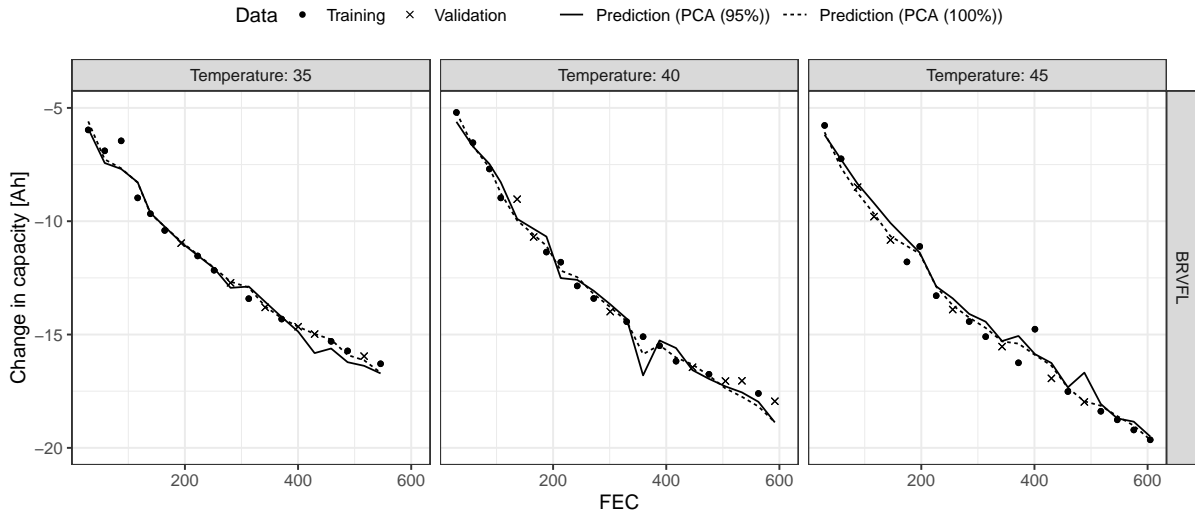
FIGURE 17. The change in capacity against FEC for each of the three temperatures in the ageing data. The dots are the measured change in capacity used to train the model, and the crosses is the measured change in capacity in the validation set. The solid and dashed curves are the changes in capacity estimated by the trained BRVFL, referring to the PCA reduced features using 95% and 100% thresholds, respectively.

are (approximately) equal, i.e.

$$\mathbb{P}_{\mathcal{S}}\left(Q^{(cy)}|\boldsymbol{S}\right) \approx \mathbb{P}_{\mathcal{T}}\left(Q^{(cy)}|\boldsymbol{S}\right). \qquad (7)$$

Because any joint distribution can be written as:

$$\mathbb{P}_{\mathcal{X}}\left(\boldsymbol{S}, Q^{(cy)}\right) = \mathbb{P}_{\mathcal{X}}\left(Q^{(cy)}|\boldsymbol{S}\right)\mathbb{P}_{\mathcal{X}}(\boldsymbol{S}),$$

the assumption of equal conditional distributions, Eq. (7), implies that the difference between the joint distributions, Eq. (6), must be due to a difference in the marginal distributions, i.e.

$$\mathbb{P}_{\mathcal{S}}(\boldsymbol{S}) \neq \mathbb{P}_{\mathcal{T}}(\boldsymbol{S}).$$

This particular type of TTL is, therefore, often called feature shifting (or more traditionally covariate shifting).

It can be shown that the difference in the marginal distributions can be accounted for by calculating importance weights for each sample in the source domain. That is, it is possible to find $\alpha(\boldsymbol{S})$ such that:

$$\alpha(\boldsymbol{S}) = \frac{\mathbb{P}_{\mathcal{T}}(\boldsymbol{S})}{\mathbb{P}_{\mathcal{S}}(\boldsymbol{S})}.$$

When the importance weights are found they are used to either up or down weight the influence of the samples in the sources domain when training a model. Training on a weighted source sample is almost identical to what was presented in Section II-C. Therefore, all that remains is to find the importance weights. However, most TTL methods require some knowledge of the marginal distribution, which may be very difficult to ascertain. A method for finding these importance weights without needing to know anything about the marginal distributions is kernel mean matching [52].

1) Kernel mean matching

Let $\mathcal{F}$ be the feature space from where the features $\boldsymbol{S}$ were sampled and $\mathcal{H}$ a reproducing kernel Hilbert space (RKHS), with the feature map $\Phi : \mathcal{F} \rightarrow \mathcal{H}$, and kernel k. Kernel mean matching (KMM) tries to estimate the importance weights, $\alpha(\boldsymbol{S})$, by minimising the maximum mean discrepancy (MMD):

$$\hat{\boldsymbol{\alpha}} = \underset{\boldsymbol{\alpha}}{\operatorname{argmin}} \,||\mathbb{E}_{\boldsymbol{S} \sim \mathbb{P}_{\mathcal{S}}}\left[\alpha(\boldsymbol{S})\Phi(\boldsymbol{S})\right] - \mathbb{E}_{\boldsymbol{S} \sim \mathbb{P}_{\mathcal{T}}}\left[\Phi(\boldsymbol{S})\right]||_2,$$

subject to:

$$\alpha(\boldsymbol{S}) \geq 0, \quad \text{and}$$
$$\mathbb{E}_{\boldsymbol{S} \sim \mathbb{P}_{\mathcal{S}}}\left[\alpha(\boldsymbol{S})\right] = 1.$$

where $||\cdot||_2$ is the ℓ_2-norm, and $\mathbb{E}_{\boldsymbol{X} \sim \mathbb{P}_{\mathcal{X}}}$ is the expected value taken w.r.t. variable $\boldsymbol{X}$ and distribution $\mathbb{P}_{\mathcal{X}}$.

Given a sample of features and their capacities from the source domain, $\mathcal{D}_{\mathcal{S}} = \{(\boldsymbol{S}_1, \Delta Q_1^{(cy)}), (\boldsymbol{S}_2, \Delta Q_2^{(cy)}), ..., (\boldsymbol{S}_N, \Delta Q_N^{(cy)})\}$, and a sample of the features from the target domain, $\mathcal{D}_{\mathcal{T}} = \{\boldsymbol{T}_1, \boldsymbol{T}_2, ..., \boldsymbol{T}_M\}$, it can be shown that MMD optimisation problem can be approximated by the following quadratic programming problem:

$$\hat{\boldsymbol{\alpha}} = \underset{\boldsymbol{\alpha}}{\operatorname{argmin}} \,\frac{1}{2}\boldsymbol{\alpha}^T K \boldsymbol{\alpha} - \boldsymbol{\kappa}^T \boldsymbol{\alpha}$$

subject to:

$$\alpha(\boldsymbol{S}_n) \in [0; U], \quad \forall n \in \{1, 2, ..., N\}, \quad \text{and}$$
$$\left|\sum_{n=1}^{N} \alpha(\boldsymbol{S}_n) - N\right| \leq N\varepsilon,$$

where U is an upper bound on the search space, ε is a normalisation error, K is a kernel matrix where $K_{ij} = k(\boldsymbol{S}_i, \boldsymbol{S}_j)$,
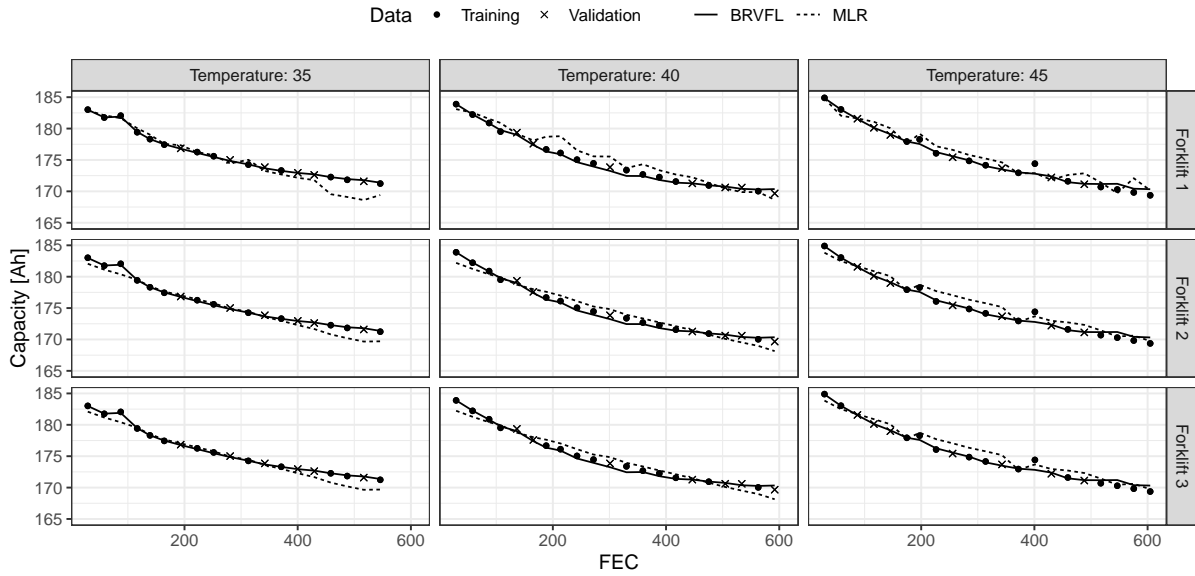
FIGURE 18. The domain transferred model evaluated on the source domain, showing the capacity against the FEC. The column shows the temperature of the source domain, while each row shows the name of the forklift used as the target domain. The dots and crosses are the points used to training and validation, respectively. Furthermore, the solid and dashed curves correspond to the estimated capacity of the domain transferred BRVFL and MLR models.

and κ is a vector where:

$$\kappa_i = \frac{N}{M} \sum_{m=1}^{M} k(\boldsymbol{S}_i, \boldsymbol{T}_m).$$

It follows that if a value κ_i is large it implies that the corresponding observation is important, leading to a large value of α_i.

In this formulation, nothing is assumed about the marginal distributions $\mathbb{P}_{\mathcal{S}}(\boldsymbol{S})$ and $\mathbb{P}_{\mathcal{T}}(\boldsymbol{S})$. In fact, the only assumptions necessary to show convergence of $\hat{\boldsymbol{\alpha}}$ to the 'true' $\boldsymbol{\alpha}$ (in this context 'true' is used in the statistical sense, i.e. the sample ratio $\hat{\boldsymbol{\alpha}}$ converges to ratio $\boldsymbol{\alpha}$ between the source and target domain) is that k needs to be universal (or equivalently strictly positive definite), and $\mathbb{P}_{\mathcal{T}}(\boldsymbol{S})$ needs to be absolutely continuous with respect to $\mathbb{P}_{\mathcal{S}}(\boldsymbol{S})$ (this ensures that $\mathbb{P}_{\mathcal{T}}(\boldsymbol{S}) = 0$ when $\mathbb{P}_{\mathcal{S}}(\boldsymbol{S}) = 0$).

III. RESULTS

The results of the transferred models will be evaluated in two ways: (1) The performance of the transferred models on the source domain, and (2) by the performance of the transferred model on the target domain. The first evaluation was included as when the model is transferred from the source to the target domain it should still perform well on the source domain. It is included as a sanity check.

A. SOURCE DOMAIN

Because there are three target domains, a total of nine combinations of sources and targets needs to be considered when evaluating the performance of the transferred model on the source domain. The results of the domain transferred models are shown in Fig. 18. The figure shows the battery

TABLE 4. The MAE and MAPE of the targeted domain transferred MLR and BRVFL on the source domain, shown for both a 95% and 100% PCA reduction thresholds and each of the three forklifts.

Forklift 1

Temperature	Method	PCA (95%)		PCA (100%)	
		MAE [Ah]	MAPE [%]	MAE [Ah]	MAPE [%]
35	MLR	5.24	3.03	1.05	0.61
40	MLR	5.41	3.16	0.75	0.43
45	MLR	2.31	1.34	0.90	0.51
35	BRVFL	4.72	2.72	0.12	0.07
40	BRVFL	5.53	3.23	0.32	0.18
45	BRVFL	4.38	2.52	0.11	0.06

Forklift 2

Temperature	Method	PCA (95%)		PCA (100%)	
		MAE [Ah]	MAPE [%]	MAE [Ah]	MAPE [%]
35	MLR	4.18	2.42	0.68	0.39
40	MLR	4.27	2.50	0.76	0.44
45	MLR	1.75	1.01	1.00	0.57
35	BRVFL	3.45	1.99	0.12	0.07
40	BRVFL	4.52	2.64	0.32	0.18
45	BRVFL	3.61	2.08	0.10	0.06

Forklift 3

Temperature	Method	PCA (95%)		PCA (100%)	
		MAE [Ah]	MAPE [%]	MAE [Ah]	MAPE [%]
35	MLR	3.19	1.85	0.68	0.40
40	MLR	3.27	1.92	0.77	0.45
45	MLR	1.40	0.80	1.01	0.58
35	BRVFL	4.05	2.34	0.11	0.07
40	BRVFL	4.97	2.91	0.31	0.18
45	BRVFL	3.92	2.26	0.11	0.06

capacity against the FEC, where each column corresponds to the temperature in the source domain, and each row corresponds to the target domain (indicated by the name of
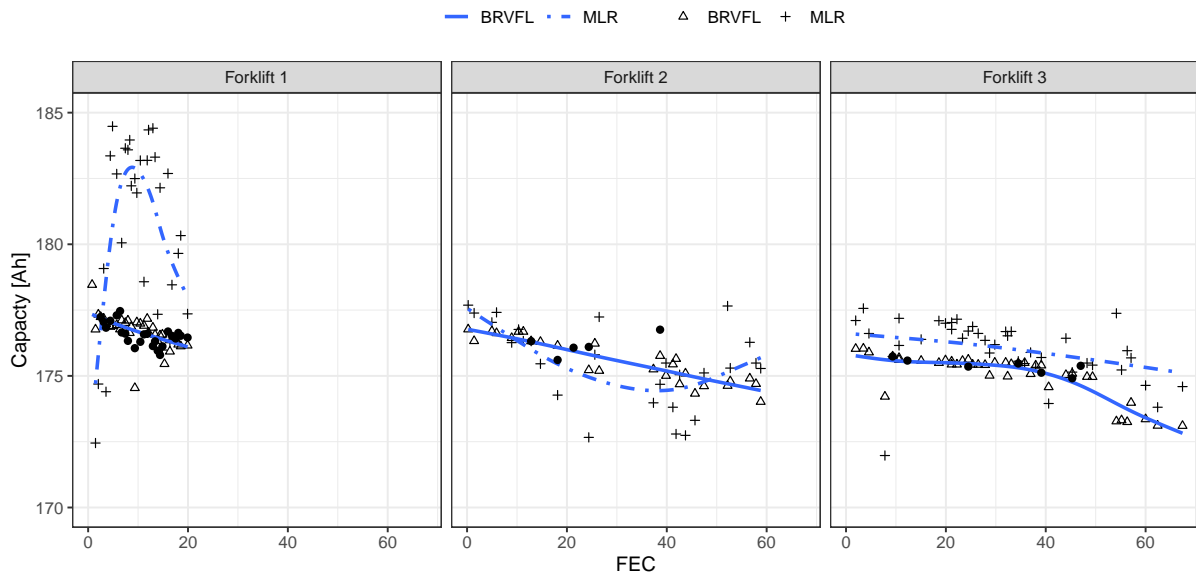
IEEE *Access*

FIGURE 19. The domain transferred model evaluated on the target domain, showing the capacity against the FEC. Each column shows the name of the forklift (the target domain). The solid and dashed curves correspond to the estimated capacity of the domain transferred BRVFL and MLR models. The black dots correspond to approximate capacity measurements of the three forklifts.

the forklift). The dots were used as the training data, while the crosses were used for validation. The dashed and solid curves correspond to the estimated capacity using the MLR and BRVFL methods, respectively. The figures show that the MLR performs poorly for a temperature of 45^oC (and for 40^oC when using Forklift 1 as a target), while being relatively accurate for 35 and 40^oC. This is not unexpected, as the temperature experienced by the forklifts is usually closer to 20^oC, increasing the importance of the samples from lower temperature sources (i.e. $\alpha(S) > \alpha(S')$ if measured temperature in $S < S'$). This is further supported by the MAE and MAPE of the validation set shown in Table 4. Focusing on the 95% PCA reduction threshold, the MAPEs are in all but three cases less than 3%. Furthermore, it is clear from the figure and table that the BRVFL is much more closely fitted to the estimated capacity of the source domain. In fact, the errors exhibited by the transferred BRVFL models are comparable to the non-transferred BRVFL models.

B. TARGET DOMAIN

The estimated SOH on the target domain was calculated in a similar fashion to the source domain, with the additional dependence of calendar ageing. Under the assumptions outlined in the beginning of Section II-C and the results of the calendar ageing model, seen in Section II-C1, it was only deemed necessary to transfer the methods modelling the change in capacity due to cycling ageing. Given the estimated change in capacity due to calendar ageing and cycling, the capacity at time w is found using Eq. (1).

The estimated capacity of the two methods on the target domain is shown in Fig. 19 against the FEC. The predictions made by transferred the MLR and BRVFL models are shown

as crosses and triangles, respectively. In addition a smoothed curve is fitted better visualise the trend of the methods, shown as the dashed and solid lines for MLR and BRVFL, respectively. Furthermore, the capacity measurements performed during the operation of the forklifts are shown as black dots. The figure shows very similar estimation results for the two methods on Forklift 2 and 3, but that the MLR method has some stability issues on Forklift 1. As a consequence, the estimated capacities of the MLR method are very far from the measured capacities on Forklift 1, while the BRVFL method is consistent through all three forklifts.

TABLE 5. The MAE and MAPE of the domain transferred MLR and BRVFL on the source target domains (i.e. the three forklifts).

Forklift	Method	MAE [Ah]	MAPE [%]
Forklift 1	MLR	4.64	2.63
Forklift 2	MLR	1.71	0.97
Forklift 3	MLR	0.45	0.26
Forklift 1	BRVFL	0.43	0.24
Forklift 2	BRVFL	0.60	0.34
Forklift 3	BRVFL	0.15	0.08

These results are also supported by finding the MAE and MAPE between instance of measured capacities and corresponding estimated capacities of the three forklifts, which can be seen in Table 5. The table shows that the BRVFL method generally outperforms the MLR method; however, if Forklift 1 is disregarded the results of the MLR still achieves MAPE's less than 1%.

IV. CONCLUSION AND DISCUSSION

The paper outlines and implements a paradigm for extracting different types of features, estimating battery SOH using cycle and calendar laboratory aging tests, and transferring the SOH estimation models to a real-life application. The methods used to parameterise the SOH estimation models based on the laboratory data, were chosen to be as simple as possible, while having good performance, narrowing the methods to multiple linear regression (MLR) and a bootstrapped variant of random vector functional link neural networks (BRVFL).

The analyses performed in the paper shows the ease of use and implementation of transfer learning for both the MLR and BRVFL methods. The transferred models showed good performance in both the source and target domains (i.e. the laboratory and field), achieving mean absolute percentage errors (MAPE's) smaller than 1% with the exception of the MLR method on a single forklift (Forklift 1).

A deviation worth pointing out is the capacity estimation results using the BRVFL method for Forklift 3 in Fig. 19. This sudden decrease while peculiar cannot be verified as no capacity measurements of the forklift exists in this period, though it is not unheard of in the literature. What further complicates matters is the fact that the decrease is not predicted by the MLR (though the variance in the prediction of the MLR increases during this period as well). Two possible scenarios could exist explaining this sharp decrease: (1) it is an actual decrease in capacity not accounted for by the MLR, this is a real possibility as the BRVFL has better performance on the source domain, or (2) it is not an actual decrease in capacity, which would imply that the BRVFL method is overfitting to the source domain. However, it is impossible to judge whether these predictions can actually be trusted without any capacity measurements.

Lastly, it is worth pointing out that this approach could be extended to involve databases of laboratory experiments with different current, SOC, and temperature profiles, as the estimated weights are used to up, or down, weight an observation dependent on the distance between the observation in the database and each observation of the field data.

REFERENCES

[1] G. Prasad and C. Rahn, "Model based identification of aging parameters in lithium ion batteries," *Power Sources*, vol. 232, pp. 79–85, 2013.

[2] L. Zheng, L. Zhang, J. Zhu, G. Wang, and J. Jiang, "Co-estimation of state-of-charge, capacity and resistance for lithium-ion batteries based on a high-fidelity electrochemical model," *Applied Energy*, vol. 180, pp. 424–434, 2016.

[3] D. Andre, M. Meiler, K. Steiner, H. Walz, T. Soczka-Guth, and D. U. Sauer, "Characterization of high-power lithium-ion batteries by electrochemical impedance spectroscopy. ii: Modelling," *Journal of Power Sources*, vol. 196, no. 12, pp. 5349–5356, 2011.

[4] M. Chen and G. A. Rincon-Mora, "Accurate electrical battery model capable of predicting runtime and I-V performance," *IEEE Transactions on Energy Conversion*, vol. 21, pp. 504–511, 2006.

[5] A. Hentunen, T. Lehmuspelto, and J. Suomela, "Time-domain parameter extraction method for thevenin-equivalent circuit battery models," *IEEE Transactions on Energy Conversion*, vol. 29, pp. 558–566, 2014.

[6] D.-I. Stroe, M. Swierczynski, A.-I. Stroe, and S. Knudsen Kær, "Generalized characterization methodology for performance modelling of lithium-ion batteries," *Batteries*, vol. 2, 2016.

[7] Stroe, A.-I., Knap, V., and Stroe, D.-I., "Comparison of lithium-ion battery performance at beginning-of-life and end-of-life," *Microelectronics Reliability*, vol. 88-90, pp. 1251–1255, 2018.

[8] D.-I. Stroe, M. Swierczynski, A.-I. Stroe, and S. Kær, "Generalized Characterization Methodology for Performance Modelling of Lithium-Ion Batteries," *Batteries*, vol. 2, no. 37, 2016.

[9] Y. Liu, Z. He, M. Gao, Y. Li, and G. Liu, "Dual Estimation of Lithium-ion Battery Internal Resistance and SOC Based on the UKF," *5th International Congress on Image and Signal Processing, Chongqing*, pp. 1639–1643, 2012.

[10] Y. Zou, X. Hu, H. Ma, and S. Li, "Combined State of Charge and State of Health estimation over lithium-ion battery cell cycle lifespan for electric vehicles," *Power Sources*, vol. 273, pp. 793–803, 2015.

[11] P.-H. Michel and V. Heiries, "An adaptive sigma point kalman filter hybridized by support vector machine algorithm for battery soc and soh estimation," in *2015 IEEE 81st Vehicular Technology Conference (VTC Spring)*, 2015, pp. 1–7.

[12] Y. Fang, R. Xiong, and J. Wang, "Estimation of Lithium-Ion Battery State of Charge for Electric Vehicles Based on Dual Extended Kalman Filter," *Energy Procedia*, vol. 152, pp. 574–579, 2018.

[13] B. Xia, Z. Lao, R. Zhang, Y. Tian, G. Chen, Z. Sun, W. Wang, W. Sun, Y. Lai, M. Wang, and H. Wang, "Online Parameter Identification and State of Charge Estimation of Lithium-Ion Batteries Based on Forgetting Factor Recursive Least Squares and Nonlinear Kalman Filter," *energies*, vol. 11, pp. 1–23, 2018.

[14] X. Sun, J. Ji, B. Ren, C. Xie, and D. Yan, "Adaptive Forgetting Factor Recursive Least Square Algorithm for Online Identification of Equivalent Circuit Model Parameters of a Lithium-Ion Battery," *energies*, vol. 12, pp. 1–15, 2019.

[15] W. Yan, B. Zhang, G. Zhao, S. Tang, G. Niu, and X. Wang, "A battery management system with a lebesgue-sampling-based extended kalman filter," *IEEE Transactions on Industrial Electronics*, vol. 66, no. 4, pp. 3227–3236, 2019.

[16] D. Xiao, G. Fang, S. Liu, S. Yuan, R. Ahmed, S. Habibi, and A. Emadi, "Reduced-coupling coestimation of soc and soh for lithium-ion batteries based on convex optimization," *IEEE Transactions on Power Electronics*, vol. 35, no. 11, pp. 12 332–12 346, 2020.

[17] L. Vichard, A. Ravey, P. Venet, F. Harel, S. Pelissier, and D. Hissel, "A method to estimate battery soh indicators based on vehicle operating data only," *Energy*, vol. 225, p. 120235, 2021. [Online]. Available: https://www.sciencedirect.com/science/article/pii/S0360544221004849

[18] V. Klass, M. Behm, and G. Lindbergh, "A support vector machine-based state-of-health estimation method for lithium-ion batteries under electric vehicle operation," *Journal of Power Sources*, vol. 270, pp. 262–272, 2014.

[19] M. Patil, P. Tagade, K. Hariharan, S. Kolake, T. Song, T. Yeo, and S. Doo, "A novel multistage Support Vector Machine based approach for Li ion battery remaining useful life estimation," *Applied Energy*, vol. 159, pp. 285–297, 2015.

[20] Q. Zhao, X. Qin, H. Zhao, and W. Feng, "State of Charge and State of Health Estimation for Lithium Batteries Using Recurrent Neural Networks," *Microelectronics Reliability*, vol. 85, pp. 99–108, 2018.

[21] X. Shu, G. Li, J. Shen, Z. Lei, and Z. Chen, "A uniform estimation framework for state of health of lithium-ion batteries considering feature extraction and parameters optimization," *Energy*, vol. 204, p. 117957, 2020.

[22] D. Liu, J. Pang, J. Zhou, Y. Peng, and M. Pecht, "Prognostics for state of health estimation of lithium-ion batteries based on combination Gaussian process functional regression," *Microelectronics Reliability*, vol. 53, pp. 832–839, 2013.

[23] R. Richardson, M. Osborne, and D. Howey, "Gaussian process regression for forecasting battery state of health," *Journal of Power Sources*, vol. 357, pp. 209–219, 2017.

[24] D. Zhou, H. Yin, P. Fu, X. Song, W. Lu, L. Yuan, and Z. Fu, "Prognostics for state of health of lithium-ion batteries based on gaussian process regression," *Mathematical Problems in Engineering*, pp. 1–1, 2018.

[25] J. Yu, "State of health prediction of lithium-ion batteries: Multiscale logic regression and Gaussian process regression ensemble," *Reliability Engineering and System Safety*, vol. 174, pp. 82–95, 2018.

[26] Z. Lyu and R. Gao, "Li-ion battery state of health estimation through gaussian process regression with thevenin model," *International Journal of Energy Research*, vol. 44, pp. 10 262–10 281, 2020.

[27] J. Jia, J. Liang, Y. Shi, J. Wen, X. Pang, and J. Zeng, "SOH and RUL Prediction of Lithium-Ion Batteries Based on Gaussian Process Regression with Indirect Health Indicators," *energies*, vol. 13, pp. 1–20, 2020.

[28] H. Feng and G. Shi, "Soh and rul prediction of li-ion batteries based on improved gaussian process regression," *Journal of Power Electronics*, pp. 1–1, 2021.

[29] D. Yang, Y. Wang, R. Pan, R. Chen, and Z. Chen, "A neural network based state-of-health estimation of lithium-ion battery in electric vehicles," *8th International Conference on Applied Energy, Energy Procedia*, vol. 105, pp. 2059–2064, 2017.

[30] J. Kim, J. Yu, M. Kim, K. Kim, and S. Han, "Estimation of Li-ion State of Health based on Multilayer Perceptron as an EV Application," *IFAC-PapersOnLine*, vol. 51, pp. 392–397, 2018.

[31] H. Chaoui and C. Ibe-Ekeocha, "State of Charge and State of Health Estimation for Lithium Batteries Using Recurrent Neural Networks," *IEEE Trans. Veh. Technol.*, vol. 66, pp. 8773–8783, 2017.

[32] G. You, S. Park, and D. Oh, "State of Charge and State of Health Estimation for Lithium Batteries Using Recurrent Neural Networks," *IEEE Trans. Ind. Electron.*, vol. 64, pp. 4885–4893, 2017.

[33] Y. Wu, Q. Xue, J. Shen, Z. Lei, Z. Chen, and Y. Liu, "State of Health Estimation for Lithium-Ion Batteries Based on Healthy Features and Long Short-Term Memory," *IEEE Access*, vol. 8, pp. 28 533–28 547, 2020.

[34] S. B. Vilsen and D.-I. Stroe, "Battery state-of-health modelling by multiple linear regression," *Journal of Cleaner Production*, vol. 290, p. 125700, 2021.

[35] W. Schmidt, M. Kraaijveld, and R. Duin, "Feedforward neural networks with random weights," in *Proceedings., 11th IAPR International Conference on Pattern Recognition. Vol.II. Conference B: Pattern Recognition Methodology and Systems*, 1992, pp. 1–4.

[36] Y. Pao, G. Park, and D. Sobajic, "Learning and generalization characteristics of random vector Functional-link net," *Neurocomputing*, vol. 6, pp. 163–180, 1992.

[37] H. Berry and M. Qupy, "Structure and Dynamics of Random Recurrent Neural Networks," *Adaptive Behavior*, vol. 14, pp. 129–137, 2006.

[38] Y. Zhang, J. Wu, Z. Cai, B. Du, and P. S. Yu, "An unsupervised parameter learning model for rvfl neural network," *Neural Networks*, vol. 112, pp. 85–97, 2019.

[39] Q. Shi, R. Katuwal, P. Suganthan, and M. Tanveer, "Random vector functional link neural network based ensemble deep learning," *Pattern Recognition*, vol. 117, p. 107978, 2021.

[40] G.-B. Huang, Q.-Y. Zhu, and C.-K. Siew, "Extreme learning machine: Theory and applications," *Neurocomputing*, vol. 70, no. 1, pp. 489–501, 2006.

[41] X. Sui, S. He, S. B. Vilsen, R. Teodorescu, and D.-I. Stroe, "Fast and Robust Estimation of Lithium-ion Batteries State of Health Using Ensemble Learning," in *2021 IEEE Energy Conversion Congress and Exposition (ECCE)*, 2021, pp. 1–8, (accepted).

[42] L. Wang, C. Pan, L. Liu, Y. Cheng, and X. Zhao, "On-board state of health estimation of lifepo4 battery pack through differential voltage analysis," *Applied Energy*, vol. 168, pp. 465–472, 2016.

[43] C. P. Lin, J. Cabrera, D. Y. W. Yu, F. Yang, and K. L. Tsui, "SOH estimation and SOC recalibration of lithium-ion battery with incremental capacity analysis & cubic smoothing spline," *Journal of The Electrochemical Society*, vol. 167, no. 9, p. 090537, 2020.

[44] X. Bian, L. Liu, and J. Yan, "A model for state-of-health estimation of lithium ion batteries based on charging profiles," *Energy*, vol. 177, pp. 57–65, 2019.

[45] X. Bian, Z. Wei, J. He, F. Yan, and L. Liu, "A novel model-based voltage construction method for robust state-of-health estimation of lithium-ion batteries," *IEEE Transactions on Industrial Electronics*, vol. 68, no. 12, pp. 12 173–12 184, 2021.

[46] Z. Wang, C. Song, L. Zhang, Y. Zhao, P. Liu, and D. G. Dorrell, "A data-driven method for battery charging capacity abnormality diagnosis in electric vehicle applications," *IEEE Transactions on Transportation Electrification*, pp. 1–1, 2021.

[47] C. She, L. Zhang, Z. Wang, F. Sun, P. Liu, and C. Song, "Battery state of health estimation based on incremental capacity analysis method: Synthesizing from cell-level test to real-world application," *IEEE Journal of Emerging and Selected Topics in Power Electronics*, pp. 1–1, 2021.

[48] X. Bian, Z. Wei, W. Li, J. Pou, D. U. Sauer, and L. Liu, "State-of-health estimation of lithium-ion batteries by fusing an open circuit voltage model and incremental capacity analysis," *IEEE Transactions on Power Electronics*, vol. 37, no. 2, pp. 2226–2236, 2022.

[49] S. Pan and Q. Yang, "A Survey on Transfer Learning," *IEEE Transactions on Knowledge and Data Engineering*, vol. 22, pp. 1345–1359, 2010.

[50] Y. Tan and G. Zhao, "Transfer Learning With Long Short-Term Memory Network for State-of-Health Prediction of Lithium-Ion Batteries," *IEEE Transactions on Industrial Electronics*, vol. 67, pp. 8723–8731, 2020.

[51] S. Kim, Y. Choi, K. Kim, and J. Choi, "Forecasting state-of-health of lithium-ion batteries using variational long short-term memory with transfer learning," *Energy Storage*, vol. 41, pp. 1–9, 2021.

[52] J. Huang, A. Smola, A. Gretton, K. Borgwardt, and B. Schölkopf, "Correcting sample selection bias by unlabeled data." in *Advances in Neural Information Processing Systems 19: Proceedings of the 2006 Conference*, vol. 19, 2006, pp. 601–608.

[53] E. Schaltz, D.-I. Stroe, K. Nørregaard, B. Johnsen, and A. Christensen, "Partial Charging Method for Lithium-Ion Battery State-of-Health Estimation," in *2019 Fourteenth International Conference on Ecological Vehicles and Renewable Energies (EVER)*, 2019, pp. 1–5.

[54] J. Meng, L. Cai, D.-I. Stroe, G. Luo, X. Sui, and R. Teodorescu, "Lithium-ion battery state-of-health estimation in electric vehicle using optimized partial charging voltage profiles," *Energy*, vol. 185, pp. 1054–1062, 2019.

[55] S. B. Vilsen, S. K. Kær, and D.-I. Stroe, "Log-Linear Model for Predicting the Lithium-ion Battery Age Based on Resistance Extraction from Dynamic Aging Profiles," *IEEE Transactions on Industry Applications*, vol. 56, no. 6, pp. 6937–6948, 2020.

[56] Daniel-Ioan Stroe, "Lifetime Models for Lithium-ion Batteries used in Virtual Power Plant Applications," Ph.D. dissertation, Aalborg University, 2014.

[57] K. P. F.R.S., "LIII. On lines and planes of closest fit to systems of points in space," *The London, Edinburgh, and Dublin Philosophical Magazine and Journal of Science*, vol. 2, no. 11, pp. 559–572, 1901.

[58] H. Hotelling, "Analysis of a complex of statistical variables into principal components," *Journal of Educational Psychology*, vol. 24, pp. 417–441, 1933.

SØREN B. VILSEN
Søren B. Vilsen recieved his B.Sc. degree in mathematics in 2013, his M.Sc. degree in applied mathematics in 2015, and his Ph.D. degree in statistics in 2018 from Aalborg University, Aalborg, Denmark. He is currently a Post. Doc. with the Department of Mathematical Sciences working closely with the Batteries research group at AAU Energy. His current research interests are statistical learning, evolutionary computation, deep learning, and sequential models with application to Lithium-based battery state estimation and lifetime prediction.
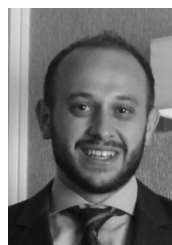
DANIEL-IOAN STROE
Daniel-Ioan Stroe received the Dipl.-Ing. degree in automatics from "Transilvania" University of Brasov, Romania, in 2008, and M.Sc. degree in wind power systems from Aalborg University (AAU), Aalborg, Denmark, in 2010. He has been with Aalborg University since 2010, from where he obtained his Ph.D. degree in lifetime modelling of Lithium-ion batteries in 2014. Currently, he is an Associate Professor with AAU Energy, where he leads the Batteries research group and the Battery Systems Testing Lab. He was a Visiting Researcher with RWTH Aachen, Germany, in 2013. He has co-authored over 150 journal and conference papers in various battery-related topics. His current research interests are in the area of energy storage systems for grid and e-mobility, Lithium-based batteries testing, modelling, diagnostics and their lifetime estimation.

• • •